ISSN 1674-1056
http://cpb.iphy.ac.cn
http://iopscience.iop.org/cpb
中国物理 B
Chinese Physics
中国物理 Chinese Physics B

Square microcavity semiconductor lasers

YueDe Yang(杨跃德), HaiZhong Weng(翁海中), YouZeng Hao(郝友增), JinLong Xiao(肖金龙), YongZhen Huang(黄永箴)
Citation: Chin. Phys. B . 2018, 27(11): 114212. **doi:** 10.1088/1674-1056/27/11/114212

Journal homepage: http://cpb.iphy.ac.cn; http://iopscience.iop.org/cpb

What follows is a list of articles you may be interested in

Electrically pumped metallic and plasmonic nanolasers

Martin T Hill
Chin. Phys. B . 2018, 27(11): 114210. **doi:** 10.1088/1674-1056/27/11/114210

Thermal analysis of GaN-based laser diode mini-array

Jun-Jie Hu(胡俊杰), Shu-Ming Zhang(张书明), De-Yao Li(李德尧), Feng Zhang(张峰), Mei-Xin Feng(冯美鑫), Peng-Yan Wen(温鹏雁), Jian-Pin Liu(刘建平), Li-Qun Zhang(张立群), Hui Yang(杨辉)
Chin. Phys. B . 2018, 27(9): 094208. **doi:** 10.1088/1674-1056/27/9/094208

High power external-cavity surface-emitting laser with front and end pump

Lidan Jiang(蒋丽丹), Renjiang Zhu(朱仁江), Maohua Jiang(蒋茂华), Dingke Zhang(张丁可), Yuting Cui(崔玉亭), Peng Zhang(张鹏), Yanrong Song(宋晏蓉)
Chin. Phys. B . 2018, 27(8): 084205. **doi:** 10.1088/1674-1056/27/8/084205

Silica-based microcavity fabricated by wet etching

H Long(龙浩), W Yang(杨文), L Y Ying(应磊莹), B P Zhang(张保平)
Chin. Phys. B . 2017, 26(5): 054211. **doi:** 10.1088/1674-1056/26/5/054211

Theoretical study of the optical gain characteristics of a $Ge_{1-x}Sn_x$ alloy for a short-wave infrared laser

Zhang Dong-Liang, Cheng Bu-Wen, Xue Chun-Lai, Zhang Xu, Cong Hui, Liu Zhi, Zhang Guang-Ze, Wang Qi-Ming
Chin. Phys. B . 2015, 24(2): 024211. **doi:** 10.1088/1674-1056/24/2/024211

TOPICAL REVIEW — Nanolasers

Square microcavity semiconductor lasers*

Yuede Yang(杨跃德), Haizhong Weng(翁海中), Youzeng Hao(郝友增), Jinlong Xiao(肖金龙), and Yongzhen Huang(黄永箴)†

State Key Laboratory of Integrated Optoelectronics, Institute of Semiconductors & College of Materials Science and Opto-Electronic Technology, University of Chinese Academy of Sciences, Chinese Academy of Sciences, Beijing 100083, *China*

(Received 9 January 2018; revised manuscript received 14 June 2018; published online 25 October 2018)

Square microcavities, which support whispering-gallery modes with total internal reflections, can be employed as high-quality laser resonators for fabricating compact, low-threshold semiconductor lasers. In this paper, we review the recent progress of square microcavity semiconductor lasers. The characteristics of confined optical modes in the square microcavities are introduced briefly. Based on the mode properties of the square microcavities, dual-mode lasers with tunable wavelength intervals are realized for generating microwave signals. Furthermore, deformed square microcavity lasers with the sidewalls replaced by circular sides are proposed and experimentally demonstrated to enhance the mode confinement and increase the dual-mode interval to the THz range. In order to further reduce the device size, metal-confined wavelength-scale square cavity lasers are also demonstrated.

Keywords: square microcavity, whispering-gallery modes, semiconductor lasers

PACS: 42.55.Sa, 42.55.Px, 42.60.Da **DOI:** 10.1088/1674-1056/27/11/114212

1. Introduction

Whispering-gallery mode (WGM) optical microcavities with merits of high quality (Q) factors, small mode volumes (V), and capability for planar integration have lots of applications in fundamental physics studies and integrated photonics devices, e.g. microlasers.[1–4] Besides the advantages of low threshold and compact size, microcavity lasers with a large value of Q/V can also promise a narrower linewidth.[5,6] WGM microcavities with circular shapes are natural choices, and have aroused great research interest due to their ultralow optical loss.[7–15] However, one major issue of these circular microcavities is the isotropic emission due to their rotational symmetry. In order to realize directional emission, an appropriate design of the microcavity shape was proposed to break the rotational symmetry and achieve efficient multi-directional or unidirectional emission while high-Q modes were preserved.[16–19] Another approach to directional emission was to add local perturbations, such as scatters, gratings, or notches, to the microcavities to efficiently modify the far-field emission patterns.[20–23]

Through optimizing the microcavity shapes or the local perturbations, directional emissions have been demonstrated with small in-plane divergence angles. However, waveguide coupling is still necessary for the practical application of microcavity lasers in photonics integrations.[24,25] The commonly used evanescent field coupling with a narrow gap between the waveguide and the microcavity may have significant difficulty in fabrication and alignment; thus, butt-coupling an output waveguide to the microcavity could be a potential solution because of the robust structure.[26] Waveguide butt-coupled microcavity semiconductor lasers were proposed and demonstrated as a potential light source in optical interconnections and photonics-integrated circuits.[27] Although high-Q coupled modes have been obtained in waveguide butt-coupled circular microcavities,[24] there is no analytical solution for the coupled modes combined by different radial-order modes, which makes the control of lasing modes more inefficient and complicated.

Besides the circular microcavities, equilateral-polygonal microcavities have also been widely investigated.[28–34] Especially for the equilateral-triangular and square microcavities, quasi-analytical solutions were obtained for the high-Q whispering-gallery-like (WG-like) modes (in the following they are also called WGMs for short).[35–38] The mode field distributions are typically very weak at the vertices in equilateral-triangular and square microcavities. Thus, butt-coupling an output waveguide to one vertex of the microcavity for unidirectional emission was proposed because the waveguide did not strongly affect the characteristics of the WGMs.[39] Here we mainly focus on the square microcavities because of their better mode confinement, sine the incident angles of the WGMs in the square microcavities are larger than those in the triangular microcavities. Square microcavities have been studied intensively over the past decades for applications in compact, low-power-consumption add-drop filters and microlasers.[40–49] For application in photonics integration, waveguide-coupled unidirectional-emission square mi-

*Project supported by the National Natural Science Foundation of China (Grant Nos. 61527823 and 61377105).

†Corresponding author. E-mail: yzhuang@semi.ac.cn

© 2018 Chinese Physical Society and IOP Publishing Ltd

crocavity semiconductor lasers have been proposed and experimentally demonstrated with various functions, such as high-speed direct modulation, single-mode operation with tunable lasing wavelength, and dual-transverse-mode lasing.[50,51]

In this paper, we review the recent progress of the square microcavity semiconductor microlasers. In Section 2, a brief introduction of the confined optical modes in the square microcavities is presented, including the analytical theories and numerical simulations. In Section 3, the experimental results on the waveguide-coupled dual-mode lasing non-deformed and deformed square microcavity lasers are provided. In Section 4, the lasing characteristics of the metal-confined wavelength-scale square cavity lasers are discussed. Finally, a summary and outlook are given in Section 5.

2. Optical modes in square microcavities

Figure 1(a) shows a typical three-dimensional (3D) square semiconductor microcavity with a vertical refractive index distribution of $n_o/n_c/n_1/n_c/n_s$. Based on the effective index approximation method, the practical 3D structure can be simplified into a two-dimensional (2D) structure by assuming a slab mode field distribution in the vertical direction. Figure 1(b) shows a simplified 2D square microcavity with a side length of a, where Ω_i and Ω_o are the inner and outer regions of the square, with refractive indices of n_i and n_o, respectively. The refractive index used in the 2D microcavity is the effective index of a multi-layer structure, which is also suitable for square microcavities with other kinds of materials. The center of the square is placed at the coordinate origin O, and thus the x and y axes are also the symmetry axes of the square. The light ray trajectory of the four-bounced mode is also indicated in Fig. 1, with the incident angle $\theta = 45°$.

An exact analytical solution can be easily obtained for the 2D circular microcavities.[9] However, for the 2D square microcavities, an analytical field distribution cannot fulfil the Maxwell's equations because of the singularity at each of the vertices. A quasi-analytical solution with sufficient precision is then required to describe the optical modes in the square microcavities.

By assuming a perfect electric or magnetic wall at the diagonals of the square for the transverse magnetic (TM) or transverse electric (TE) mode, correspondingly, a theoretical model was presented for the four-bounced high-Q WGMs in the square microcavity.[52] The analytical results agreed well with finite-difference time-domain (FDTD) numerical simulation results, and the free spectrum ranges of the high-Q WGMs in square microcavities were found to be twice those in circular microcavities of a similar size.[53] All the confined optical modes were described with a semi-classical model similar to the Marcatili's scheme that was used to analyze the rectangular waveguide, by assuming that the internal field is sinusoidally or cosinoidally oscillated along the x and y axes while the external field decays exponentially.[31] Although the external field obtained by the analytical model is incorrect, the internal field is expected to be sufficiently precise since it satisfies Maxwell's equations inside the microcavity and at the boundaries except for four vertices. The far-field emission method was used to calculate the external field and estimate the modal loss based on the analytical internal field distribution.[35]

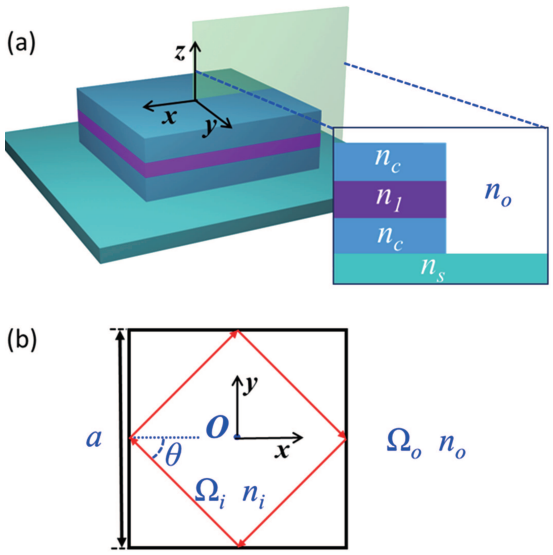


Fig. 1. (color online) (a) 3D and (b) 2D schematic diagrams of a square optical microcavity.

The TE (TM) confined modes in the square microcavities modes are denoted as $\mathrm{TE}_{p,q}$ ($\mathrm{TM}_{p,q}$), where the mode numbers p and q are used to denote the node numbers of the H_z (E_z) wave in the x and y directions, respectively. The high-Q WGMs, which correspond to the superposition of the doubly degenerate modes, have field distributions with odd parity relative to the diagonal. The formed high-Q WGM was first explained as the C_{4v} symmetry of the square with the group theory,[30] and then the physical mechanism was explained by the mode coupling theory.[37] The mode coupling between the doubly degenerate modes $\mathrm{TE}_{p,q}$ and $\mathrm{TE}_{q,p}$ ($\mathrm{TM}_{p,q}$ and $\mathrm{TM}_{q,p}$) results in the high-Q WGM marked by $\mathrm{TE}^{\mathrm{o}}_{p,q}$ ($\mathrm{TM}^{\mathrm{o}}_{p,q}$) since p and q have the same parity, where "o" indicates the odd parity relative to the diagonal. Figures 2(a)–2(d) show the magnetic field ($|H_z|$) distributions of the high-Q WGMs $\mathrm{TE}^{\mathrm{o}}_{20,22}$, $\mathrm{TE}^{\mathrm{o}}_{19,23}$, $\mathrm{TE}^{\mathrm{o}}_{18,24}$, and $\mathrm{TE}^{\mathrm{o}}_{17,25}$, respectively. The high-Q WGMs exhibit sinusoidally modulated envelopes along the sidewalls of the square microcavities. The transversal mode number m of the WGM is then defined as the node number of the envelope along the sidewalls with $m = |p-q|/2-1$, and the longitudinal mode number l is defined as $l = p+q$. Thus $\mathrm{TE}^{\mathrm{o}}_{20,22}$, $\mathrm{TE}^{\mathrm{o}}_{19,23}$, $\mathrm{TE}^{\mathrm{o}}_{18,24}$, and $\mathrm{TE}^{\mathrm{o}}_{17,25}$ shown in Fig. 2 correspond to the fundamental, first-order, second-order, and third-order transverse order WGMs with the same longitudinal mode number. Due to the sinusoidally

modulated field distribution envelopes, an output waveguide butt-coupled to the position of the envelope node can be used to realize waveguide-coupled unidirectional-emission without degrading the mode Q factor. The mode characteristics of the optical modes in square microcavities were comprehensively studied in Ref. [51]. In the square semiconductor microcavity, the mode coupling can suppress the optical loss greatly, and result in a high-Q WGM. However, if the refractive index ratio n_i/n_o is close to $\sqrt{2}$, the loss channels of the modes (p, q) and (q, p) are much different, and thus the modal loss cannot be canceled by the mode coupling. Since none of boundary wave leakage losses from the vertices are sensitive to the cavity size, we expect that the mode Q is approximately proportional to the area of the 2D square microcavity.

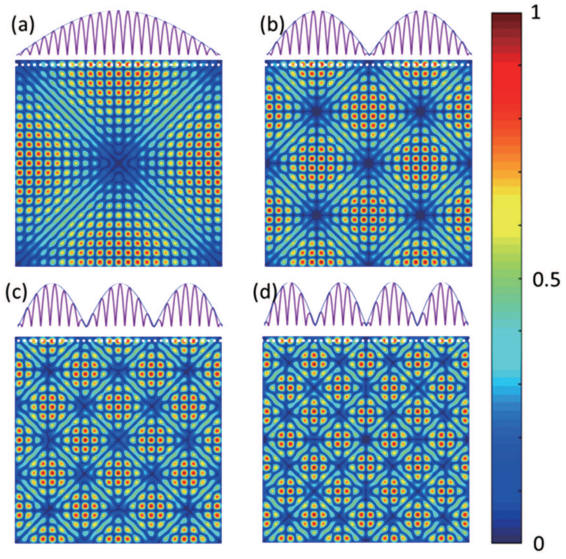


Fig. 2. (color online) Magnetic field distributions for the (a) fundamental, (b) first-order, (c) second-order, and (d) third-order transverse order TE WGMs in square microcavities.

The WGMs in the circular microcavities are doubly degenerate modes because of the rotational symmetry. In the square microcavities, the mode coupling removes the doubly degenerate properties for part of the confined modes, and results in nondegenerate high-Q WGMs in the square microcavities, which is essential to achieve real single-mode operation for the microcavity laser.[30] However, the standing wave property of the high-Q WGM makes the square microcavity unsuitable for realizing efficient optical add-drop filters. A deformed square microcavity with cut and circular corners was proposed to realize a traveling wave-like filtering response.[43]

For a 3D square microcavity, theoretical analysis is complicated. Thus, a 2D square microcavity is typically considered by simplifying the 3D structure into a 2D structure. For the square microcavity vertically confined by a semiconductor material with a low contrast of refractive index, the 2D model will give an incorrect high-Q factor since the vertical radiation loss is neglected.[54] However, the 2D model is still a powerful tool because it can predict a high-Q WGM and provide an accurate mode structure more efficiently than the 3D model. The vertical radiation loss can be explained as the coupling between the WGM and vertical propagation mode, and becomes the dominant loss in the square microcavity with a side length of a few microns for the TE mode.[10] In order to achieve the high-Q mode in a wavelength-scale square microcavity, a metal layer is usually introduced to enhance the light confinement in vertical and horizontal directions.

Based on the theoretical analyses and numerical simulations of the mode characteristics, a square microcavity semiconductor laser with the waveguide butt-coupled to one vertex or the midpoint of one side was proposed for unidirectional emission. A single-mode square microcavity laser with a tunable lasing wavelength and the capability for high-speed direct modulation has been experimentally demonstrated, with the lasing characteristics in good agreement with those from the quasi-analysis model and the numerical simulation.[51] The mode properties of a square microcavity allow stable dual-mode lasing in a single laser cavity, and the corresponding recent experimental results are presented below.

3. Dual-mode square microcavity semiconductor lasers

Dual-wavelength semiconductor lasers have been extensively studied because of their potential applications in microwave and THz wave generation. If the dual wavelength emission can be achieved in a single laser cavity, a microwave or THz wave source with simplified structure and stabilized operation can then be realized. Based on the spatially separated field distribution between nearby high-Q WGMs, dual-wavelength lasing has been demonstrated in square microcavity lasers.[55] In this section, we review the recent experimental results on the dual-mode square microcavity lasers.

3.1. Tunable wavelength intervals in dual-transverse-mode square microcavity lasers

For an AlGaInAs/InP square microcavity with a side length (a) of 30 μm and a refractive index (n_1) of 3.2, which equals the effective index of the AlGaInAs/InP multiple-quantum-well (MQW) epitaxial wafer used in the experiment, surrounded by a thin SiN_x layer and divinylsiloxane bisbenzocyclobutene, an output waveguide with a width (w_g) of 2.5 μm was butt-coupled to one vertex of the square microcavity for realizing waveguide-coupled unidirectional emission. Figures 3(a) and 3(b) show the magnetic field (H_z) distribution of the fundamental WGM $TE^o_{86,88}$ and the first-order WGM $TE^o_{85,89}$ obtained by the FDTD simulations, respectively. The WGMs $TE^o_{86,88}$ and $TE^o_{85,89}$ have mode wavelengths of 1553.85 nm and 1553.58 nm with Q factors of 1.46×10^5 and 5.52×10^4, respectively. The arrowed lines

in Figs. 3(a) and 3(b), which connect the midpoints and the quarter points of the adjacent sides of the square microcavity, respectively, indicate the optical light trajectories of the main mode field for the WGMs $TE^{o}_{86,88}$ and $TE^{o}_{85,89}$. Dual-transverse-mode lasing is expected because the modal loss is very similar to a difference less than 2 cm^{-1} and the mode field distributions are spatially separated.

Figure 3(c) shows a 2D schematic diagram of the waveguide-coupled square microcavity laser with a square-ring-shaped injection window, where a square-ring-shaped contact window connecting the midpoints has been designed to inject the current nonuniformly. The width of the injection window (W) is 4 μm. The nonuniform current injection can modulate the carrier and temperature distributions inside the laser cavity and build up a refractive index step around the injection window. Because the main mode field distributions of the fundamental and first-order modes are matched and mismatched with the injection window, respectively, and the wavelength variation of the fundamental mode will be larger than that of the first-order mode when a refractive index change is built up within the injection window, the wavelength interval between the two lasing modes can be tuned by varying the injection current.[55]

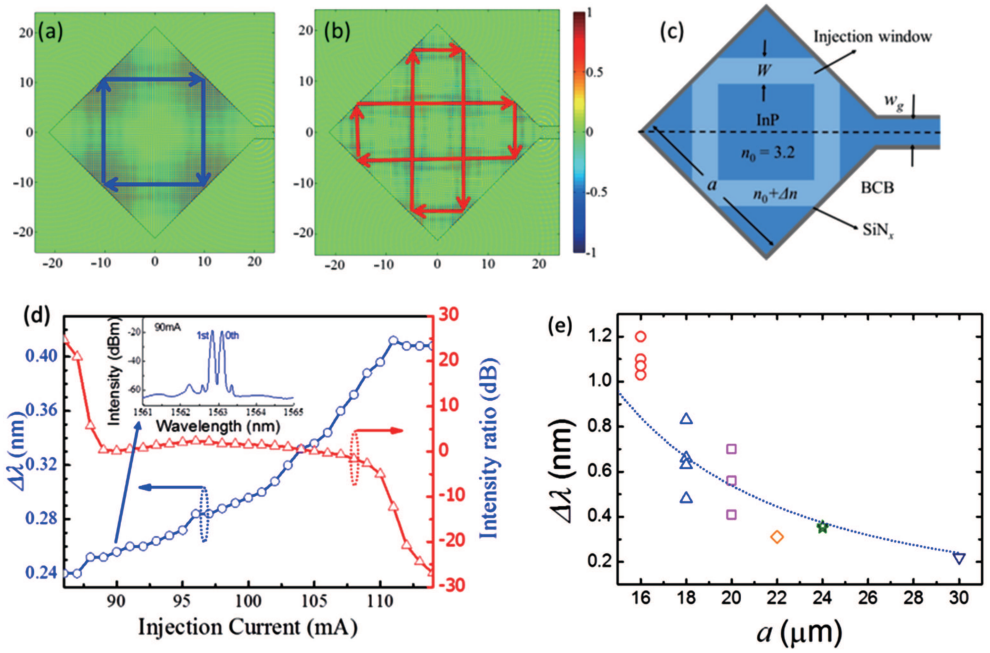


Fig. 3. (color online) Magnetic field distributions of the (a) fundamental and (b) first-order transverse TE WGMs. (c) Schematic diagram of waveguide-coupled square microcavity laser with square-ring-shaped injection window. (d) Wavelength interval and intensity ratio between two lasing modes versus injection current, with inset showing the lasing spectrum at an injection current of 90 mA. (e) Wavelength interval versus side length of square microlaser.

A square microcavity laser with parameters similar to those used in the FDTD simulations was fabricated on an AlGaInAs/InP MQW epitaxial wafer by using the fabrication process similar to that in Ref. [51]. A tapered single-mode fiber (SMF) butt-coupled to the cleaved end of the output waveguide was used to collect the laser output light. Lasing spectra were measured by an optical spectrum analyzer with a resolution of 0.02 nm at room temperature under different continuous injection currents. The wavelength interval and the intensity ratio between the fundamental (0^{th}) and first-order (1^{st}) transverse modes can be extracted from the lasing spectra. The inset in Fig. 3(d) shows the measured lasing spectrum at an injection current of 90 mA. Figure 3(d) shows the obtained wavelength interval and the intensity ratio versus injection current. When the injection current increases from 89 mA to 110 mA, the intensity ratio is always less than 3 dB and the wavelength interval $\Delta\lambda$ increases from 0.25 nm to 0.39 nm. The corresponding frequency difference between the two lasing modes is in a range from 30 GHz to 48 GHz.

The transverse mode wavelength interval $\Delta\lambda_t$ between the fundamental and first-order modes can be obtained from a quasi-analytical modal to be $\Delta\lambda_t = 3\lambda^3/(4n_g^2a^2)$.[51] The transverse mode wavelength interval is inversely proportional to the cavity area a^2, while the longitudinal mode wavelength interval is inversely proportional to the side length a. Thus, the decrease in cavity size can greatly enhance the wavelength interval of dual-transverse-mode square microcavity lasers. Figure 3(e) shows a plot of the wavelength interval versus side length of the square microcavity laser with a uniform current injection, where the dotted line indicates the analytical wavelength interval with the group refractive index $n_g = 3.6$ around 1550 nm. However, the first-order transverse mode stops lasing when $a < 16$ μm because of the excessive lowering of the Q factor by the butt-coupled waveguide.

3.2. Lasing spectrum control for deformed square microcavity laser

In order to further enhance the wavelength interval of the dual-transverse-mode square microcavity laser, we proposed and demonstrated deformed square microcavities with their flat sides replaced by circular sides.[56] Figure 4(a) shows a schematic diagram of a deformed square microcavity laser with the flat sides replaced by circular sides, where a is the side length of the square, δ is the deformation parameter, and r is the radius of the circular side. Considering the mode field distributions of the fundamental and first-order transverse modes as shown in Figs. 3(a) and 3(b), the effective round-trip length of the fundamental mode will be longer than that of the first-order mode in the circular-sided square microcavity. Thus, with the increase in deformation parameter δ, the wavelength of the fundamental mode should increase much faster than that of the first-order mode, and the wavelength interval should be enhanced greatly.

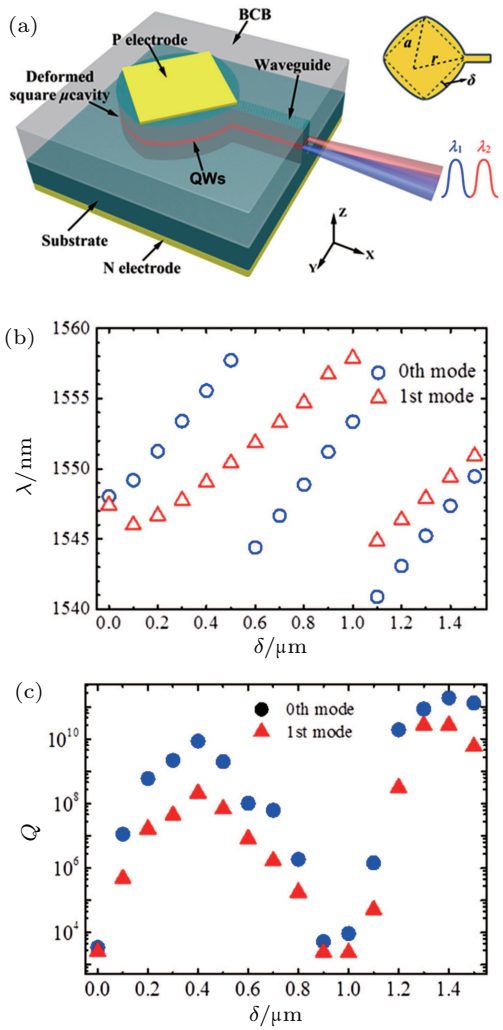


Fig. 4. (color online) (a) Schematic diagram of waveguide-coupled circular-sided square microcavity laser. (b) Mode wavelengths and (c) corresponding mode Q factors for the WGMs around 1550 nm versus deformation amplitude δ.

High-Q WGMs in circular-sided square microcavities are numerically simulated by a 2D finite element method (FEM). TE WGMs with magnetic field (H_z) distributions symmetric with respect to the middle line of the output waveguide are considered here. For the circular-sided square microcavity with $a = 16$ μm and output waveguide width $w = 1.5$ μm, plots of mode wavelength and Q factor versus δ obtained by the FEM are shown in Figs. 4(b) and 4(c) for the fundamental (0^{th}) and first-order (1^{st}) transverse modes. The mode wavelength of the fundamental transverse mode redshifts about 17 nm as δ increases by 0.1 μm due to the increase in the effective cavity size (or the effective round-trip length), which is close to the longitudinal-mode wavelength interval $\Delta\lambda_l$. The wavelengths of the fundamental, first-order, and transverse modes shown in Fig. 4(b) are kept around 1550 nm by choosing different longitudinal modes. Because the WGMs have the same longitudinal mode number, the transverse mode intervals increase gradually as deformation parameter δ increases; this is due to the increase in the effective round-trip length difference. However, if $\Delta\lambda_t > \Delta\lambda_l/2$, the wavelength interval between the near fundamental and first-order transverse modes becomes $\Delta\lambda = \Delta\lambda_l\Delta\lambda_t$. Then, the wavelength interval will decrease with increasing δ when $\delta > 0.6$ μm, as shown in Fig. 4(b). The mode Q factors of the fundamental and first-order order transverse modes are 8.7×10^9 and 2.1×10^8 at $\delta = 0.4$ μm, and are 1.9×10^{11} and 2.7×10^{10} at $\delta = 1.4$ μm, respectively, which are much larger than those in a square microcavity. The mode Q factors are low around $\delta = 0.95$ μm because there are no long-life light rays according to the light ray simulation.[56]

Like the AlGaInAs/InP square microcavity laser, the circular-sided square microcavity laser was fabricated on the AlGaInAs/InP MQW epitaxial wafer with parameters similar to those used in the simulation ($a = 16$ μm and $w = 1.5$ μm). The inset in Fig. 5(a) shows a top-view optical microscope image of a fabricated circular-sided square microcavity laser. Figure 5(a) shows the lasing spectrum for a circular-sided square microcavity laser with $\delta = 1.1$ μm. Dual-mode lasing with a wavelength interval of 3.43 nm is obtained to have a side-mode-suppression ratio (SMSR) of 26 dB and an intensity ratio of about 0.4 dB. The fundamental and first-order transverse modes are marked by circles and triangles, respectively. Unlike the nondeformed square microcavity laser, the fundamental lasing mode is on the short wavelength side because the two lasing modes have different longitudinal mode numbers. Figure 5(b) shows the wavelength intervals of the circular-sided square microcavity lasers with different values of δ. Since the fundamental mode is on the long-wavelength side when $\delta < 0.7$ μm, as shown in Fig. 4(b), $\Delta\lambda$ first increases with δ, and a wavelength interval of 7.6 nm is achieved at $\delta = 0.7$ μm. The wavelength interval can be larger than half of the longitudinal mode interval by varying the injection

current to control the gain spectrum. As δ increases beyond 1.1 μm, $\Delta\lambda$ decreases because the fundamental mode is on the short-wavelength side and moves towards the first-order mode.

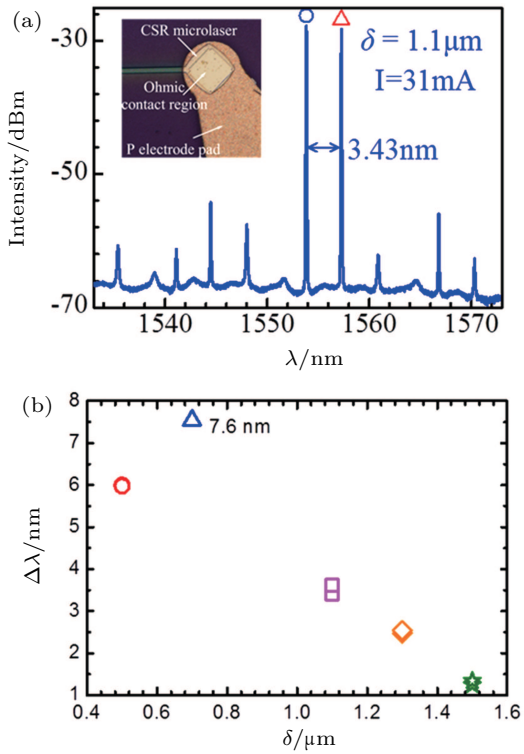


Fig. 5. (color online) (a) Lasing spectrum for the circular-sided square microcavity laser with $\delta = 1.1$, with inset showing an optical microscope image of the circular-sided square microlaser. (b) Plot of wavelength interval versus δ of circular-sided square microcavity laser.

The experimental results indicate that dual-mode lasing can be easily realized in the circular-sided square microcavity with the ultrahigh-Q mode, and the transverse mode interval can be adjusted by varying the deformation parameter δ. The wavelength interval between the lasing modes is also limited by the longitudinal mode interval due to the lasing mode competition.

Nonlinear gain analyses of a density matrix formalism are performed to describe the stability of dual-mode lasing for the nondeformed and deformed square microcavity lasers, respectively. In the nondeformed square microcavity, the mode field patterns are determined by two mode numbers p and q along the directions of the square sides according to the quasi-analytical model. The p and q are different for the near high-Q WGMs, and therefore stable dual-mode lasing can be expected for the square microcavity laser. In the deformed square microcavity with circular-sides[56] or variable curvature,[57] the overlap of mode field intensities between even the near high-Q WGMs is less than that of the non-deformed square microcavities according to the numerical simulations. Thus, stable dual-mode lasing can also be achieved for the deformed square microcavity laser with an enhanced wavelength interval.

3.3. Microwave and sub-THz wave generation based on square microcavity laser

Microwave signal generation has been demonstrated directly from the square microcavity laser subjected to external optical injection,[58] and also by the optoelectronic oscillator with a directly modulated square microcavity laser.[59] However, the frequency of the generated microwave signal is limited by the modulation bandwidth of the directly modulated square microcavity laser. Based on the dual-mode lasing nondeformed and deformed square microcavity lasers, the signal frequency can be extended from tens of GHz to the THz through mode beating.[55,56] We have demonstrated sub-THz wave generation based on the dual-mode square microcavity laser and the uni-travelling-carrier photodiode (UTC-PD), and the obtained signal frequency is mainly limited by the response bandwidth of the UTC-PD.[60]

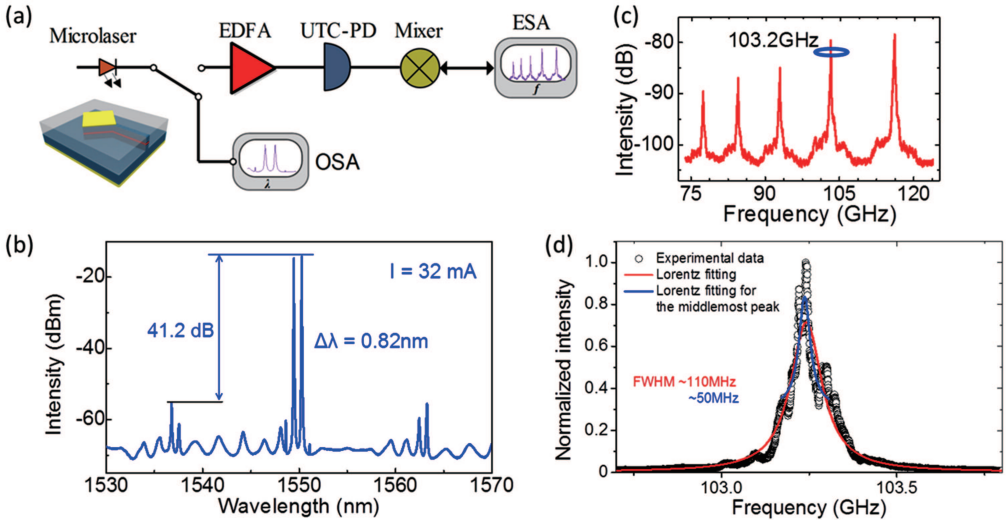


Fig. 6. (color online) (a) Experimental setup for THz wave generation using dual wavelength square microlaser. (b) Lasing spectrum at an injection current of 32 mA. (c) Original mixed frequency signal. (d) Detailed electrical spectra around 103.2 GHz.

An 18 μm-side-length square microcavity laser with a 1.5 μm-wide output waveguide was used in the experiment of sub-THz signal generation. Figure 6(a) shows a schematic diagram of the experimental setup with a dual-mode square microcavity laser. The output light from the square microcavity laser was coupled by a tapered SMF and amplified by an erbium-doped fiber amplifier with a gain of 32 dB, and was then applied to the UTC-PD mixer. The output electrical signal from the mixer was fed into an electric spectrum analyzer with a harmonic mixer. Figure 6(b) shows the optical spectrum of the square microcavity laser under an injection current of 32 mA. The two main lasing peaks have a wavelength interval of 0.82 nm and an intensity ratio of about 0.5 dB. The lasing spectrum indicates the simultaneous lasing of the fundamental and first-order transverse modes with an SMSR of about 41.2 dB. Figure 6(c) shows the generated sub-THz signal at the UTC-PD mixer with the dual-mode square microcavity laser under the same injection current, which indicates a center frequency of 103.2 GHz for the beating signal. The other peaks are induced by the local oscillator in the frequency mixer. Figure 6(d) shows the detailed electrical spectra for the generated sub-THz wave signal around 103.2 GHz, fitted with different methods. A linewidth of about 110 MHz is obtained according to a Lorentz fitting. The linewidth is defined as the full-width at half-maximum. However, the signal linewidth is broadened due to the system's instability and/or signal drifting. Using Lorentz fitting with a smaller range for the middlemost peak, the linewidth is obtained to be about 50 MHz, as shown in Fig. 6(d), which is supposed to be the actual linewidth.

3.4. Spectra linewidth analysis for a dual-mode square microcavity laser

A dual-mode microcavity laser can not only simplify the structure but also stabilize the operation since two modes lase in a single cavity. The two lasing modes may have a relation in the phase, which is beneficial to the microwave or THz wave signal generation and to the optical frequency comb generation through four-wave mixing. We have demonstrated a strong correlation between the two lasing modes in the dual-mode square microcavity laser.[61]

A dual-mode square microcavity laser with a side length of 20 μm and a 1.5 μm-wide output waveguide was used in the experiment for spectrum linewidth analysis. Figure 7(a) shows the dual-mode lasing spectrum at an injection current of 50 mA. The left inset in Fig. 7(a) shows the detailed spectrum around the main peaks after a pre-amplifier and a band-pass filter. The lasing peaks at 1560.03 nm and 1559.74 nm are the fundamental (0^{th}) and first-order (1^{st}) transverse modes, respectively, and the corresponding wavelength interval is 0.29 nm. Combining the amplified laser light of the square microcavity laser with that from a narrow linewidth (∼ 100 kHz) TLS, the detailed spectrum is shown in the right inset in Fig. 7(a). The combined laser light is detected by a 30 GHz high-speed photodiode. Figure 7(b) shows the measured electrical spectrum. Three main microwave peaks at 11.16 GHz, 24.76 GHz, 35.91 GHz are obtained, corresponding to the beating signals between the TLS and the first-order mode (S_{T1}), between the TLS and the fundamental mode (S_{T0}), and between the two lasing WGMs (S_{01}), respectively. Two other small peaks at 13.51 GHz and 22.27 GHz are also observed, which result from the microwave mixing effect.

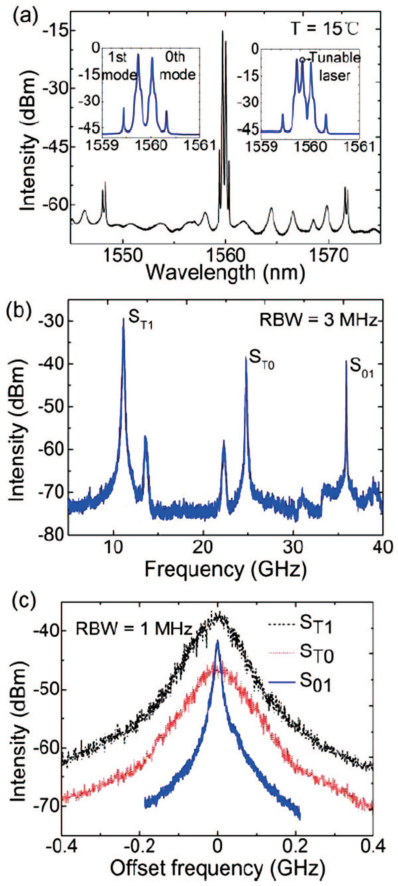


Fig. 7. (color online) (a) Dual-mode lasing spectrum at 50 mA for a dual-mode square microcavity laser with a side length of 20 μm. Left inset: spectrum after amplifier and filter. Right inset: combined spectrum of the dual-mode and a TLS. (b) Measured beating signal of the combined optical spectrum. RBW: resolution bandwidth. (c) Zoomed-in electrical spectra. Reproduced from Ref. [61].

Figure 7(c) shows the zoomed-in electrical spectra of the three main peaks, where S_{01} has a much narrower linewidth than S_{T0} and S_{T1}. The linewidths of S_{01}, S_{T1}, and S_{T0} are 12 MHz, 88 MHz, and 102 MHz, respectively, according to the Lorentzian fitting. Because the linewidth of the TLS is about three orders smaller than that of S_{T1} and S_{T0}, the linewidths of S_{T1} and S_{T0} are approximately those of the lasing WGMs. The linewidth of S_{01} is much narrower than that of S_{T1} and S_{T0} because the phase noise caused by the carrier fluctuation may be synchronized for the two lasing modes in the dual-mode square microcavity laser. In addition, the nonlinear process

between the two WGMs will also make the two modes more correlated. Thus, the experimental results prove that a strong correlation exists between the two lasing modes.

4. Wavelength and subwavelength scale metallic square cavity semiconductor lasers

Besides the dual-mode laser used in the microwave or THz wave generation, wavelength or subwavelength scale semiconductor lasers with ultralow power consumption are greatly demanded for applications in on-chip optical interconnects. We have demonstrated room-temperature lasing for an aluminum/silica coated AlGaInAs/InP square cavity under optical pumping.[62]

Figure 8(a) shows a schematic diagram of the wavelength-scale square cavity semiconductor laser, which consists of a square cross-section semiconductor core with an AlGaInAs MQW gain layer coated by aluminum/silica on the bottom and sidewalls. The AlGaInAs/InP epitaxial laser wafer was first etched to a depth of about 1.2 μm by the inductively coupled plasma dry etching technique, with a patterned SiO_2 layer used as a hard mask. The etched square microcavity was coated by the silica and aluminum layers with the same thickness of 200 nm, and then bonded on a silicon wafer by using BCB adhesive bonding technology. Finally, the InP substrate was removed by a wet etching process, with a 200 nm thick InGaAsP used as the etching stop layer. Figure 8(b) shows the top-view SEM image of a fabricated wavelength-scale square cavity laser with a side length of about 2.2 μm, where the inset shows a tilted view SEM image of the square cavity.

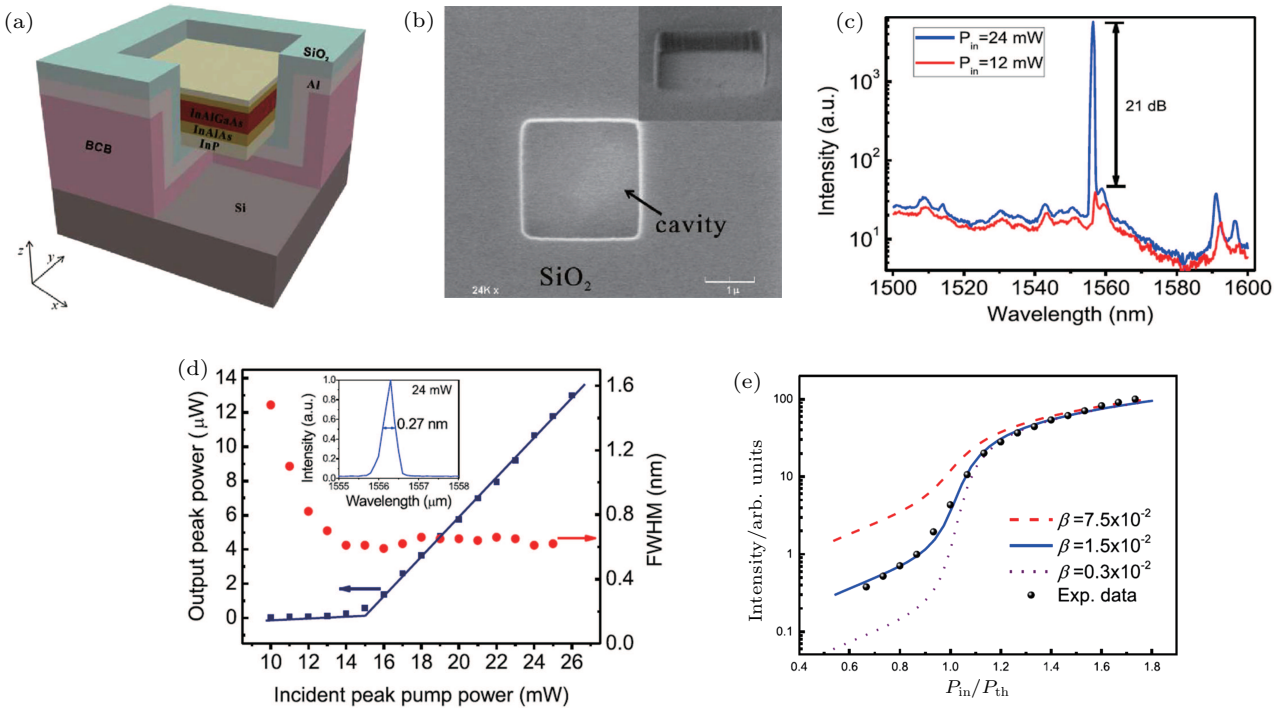


Fig. 8. (color online) (a) Schematic diagram of aluminum/silica wavelength-scale square cavity laser. (b) SEM image of fabricated square cavity laser with a side length of about 2.2 μm, with the inset showing a tilted view of the cavity. (c) Room temperature lasing spectra for the square cavity laser. (d) Output peak power and linewidth of the lasing mode versus incident peak pump power for the square cavity laser, with the inset showing the detailed lasing spectrum. (b) Theoretical curves and the experimental results of laser mode power against input pump power. Reproduced from Ref. [62].

The AlGaInAs/InP square laser with a side length of 2.2 μm was tested at room temperature (293 K) by a microphotoluminescence setup with a 976 nm pulsed laser source. The pulse width was 60 ps with a repetition rate of 20 MHz. A 40× objective lens was used to focus the pumping laser beam on the AlGaInAs/InP square laser with a spot diameter of 4 μm and simultaneously collect the emitting light. Figure 8(c) shows the measured output spectra at the pumping peak powers of 12 mW and 24 mW, which correspond to the states below and above the lasing threshold, respectively. The laser spectrum indicates single mode lasing at the wavelength of 1556.5 nm with an SMSR of 21 dB at the peak pumping power $P_{in} = 24$ mW.

Figure 8(d) shows the output peak power and the linewidth of the lasing mode as a function of incident peak pumping power, which indicates a threshold peak pump power of 15 mW. Assuming that the absorption coefficient is 10^4 cm^{-1} in the InAlGaAs layer, the absorbed peak threshold power is estimated as 1–2 mW. The corresponding effective threshold pumping intensity is 20–40 kW cm^{-2}. The linewidth of 0.65 nm above the threshold is limited by the resolution of the monochromator with a slit width of 200 μm, which is used to enhance the signal-to-noise ratio below threshold. The inset of Fig. 8(d) shows the lasing spectrum measured with a 50

μm wide slit and $P_{in} = 24$ mW, which indicates a linewidth of 0.27 nm. The measured linewidth is mainly limited by the slit width because of the low output power.

Figure 8(e) shows the intensity of the lasing mode versus peak power of the pulsed pumping laser, which is denoted by the solid circles. The input power P_{in} and the output power are proportional to the integration of $P(t)$ and the mode photon density over a period, respectively. Taking a mode Q factor of 1300 as a lasing mode, which is obtained by the 3D FDTD simulation, the laser mode power against input pump power normalized by the threshold pump power can be obtained by the rate equation model. The obtained results with different values of spontaneous emission factor β are shown in Fig. 8(e) as dashed, solid, and dotted lines, respectively. It can be found that the lasing output curve of the lasing mode at 1556.5 nm can be fitted very well with the simulation results at $\beta = 1.5 \times 10^{-2}$. The spontaneous emission factor can be enhanced by further reducing the cavity size with metal confinement.

By further reducing the cavity size from the wavelength scale to subwavelength scale, the mode Q factor decreases from 10^3 to a few hundred. The bulk material active layer is then required to provide sufficient saturation gain to balance the high modal loss, which may result in high injection current density and hence large heat generation. An electrical injection Ag/SiN-coated rectangular cavity semiconductor laser with a modal volume of $0.67\lambda^3$ was demonstrated at room temperature.[63,64] The mode Q factor obtained by the FDTD simulation was 428 for the rectangular cavity, and the linewidth was 0.5 nm for the laser above threshold. The threshold current was 1.1 mA, corresponding to a current density of 60 kA/cm^2. The spontaneous emission factor β was 0.05 based on the light output curve. The processing techniques and device designs need further optimization to reduce the threshold current density for practical application.

In order to break the diffraction limit, plasmon lasers have been proposed and demonstrated as a new class of coherent compact light sources.[65,66] Subdiffraction-limited square plasmon laser was realized at room temperature under optical pumping.[46] A 45 nm thick and 1 μm long CdS square was located on the silver surface with a 5 nm MgF_2 gap, thereby forming a square plasmon laser. The TM modes confined at the metal–dielectric interface resulted in strong light confinement in the gap region with relatively low loss, while the TE modes exhibited large radiation losses. With the help of surface plasmon polaritons, the diffraction limit in the vertical direction was broken. The light in the horizontal direction was still confined by the total reflection at the boundaries, with the field distribution similar to that of the WGMs in a dielectric square microcavity.

5. Summary and outlook

In summary, we have reviewed the recent progress of square microcavity semiconductor lasers. High-Q WGMs in square optical microcavities are introduced briefly for realizing unidirectional emission and achieving mode control. Based on the unique mode properties of the square microcavities, dual-mode microlasers with a tunable wavelength interval are demonstrated experimentally using a spatially selective current injection. Deformed square microcavities with the flat sidewalls replaced by circular arcs are proposed and demonstrated for enhancing the mode confinement and increasing the dual-mode interval from tens of GHz to the THz range. In order to further reduce the laser size, wavelength-scale square cavity lasers are also demonstrated with aluminum/silica layers to confine the mode field close to the diffraction limit.

In the circular-shaped optical microcavities, WGMs distribute uniformly along the cavity rim within a very narrow region. In contrast, high-Q WGMs in square microcavities typically distribute over the whole cavity with a sinusoidal envelope along the sidewall. Due to the large offset of the field distributions between different transverse modes, the modulation and control of the lasing mode can be achieved by designing the output waveguide and spatially selective injection. The widely distributed mode field can also promise high injection efficiency and avoid burning-induced diffusion in high-speed direct modulation. According to these novel properties of the square optical microcavity, we have already demonstrated different functional square semiconductor microlasers. Besides the semiconductor laser with a single square cavity, the twin-square coupled microcavity laser was demonstrated for the enhancement of modulation bandwidth due to the photon–photon resonance effect,[67] and the square-rectangular coupled cavity laser was demonstrated for single-mode lasing with tunable wavelength[68] and high-speed flip-flop.[69] We believe that the performance of square microcavity semiconductor lasers can be further improved, and then practical application can be realized.

References

[1] Vahala K J 2003 *Nature* **424** 839
[2] He L N, Ozdemir S K and Yang L 2013 *Laser Photon. Rev.* **7** 60
[3] Cao H and Wiersig J 2015 *Rev. Mod. Phys.* **87** 61
[4] Jiang X F, Shao L B, Zhang S X, Yi X, Wiersig J, Wang L, Gong Q H, Loncar M, Yang L and Xiao Y F 2017 *Science* **358** 344
[5] Bulovic V, Kozlov V G, Khalfin V B and Forrest S R 1998 *Science* **279** 553
[6] Jiang X F, Zou C L, Wang L, Gong Q H and Xiao Y F 2016 *Laser Photon. Rev.* **10** 40
[7] Mccall S L, Levi A F J, Slusher R E, Pearton S J and Logan R A 1992 *Appl. Phys. Lett.* **60** 289
[8] Fujita M, Ushigome R, Baba T, Matsutani A, Koyama F and Iga K 2001 *Jpn. J. Appl. Phys.* **40** 5338
[9] Yang Y D, Huang Y Z and Chen Q 2007 *Phys. Rev. A* **75** 013817
[10] Huang Y Z and Yang Y D 2008 *J. Light. Technol.* **26** 1411

[11] Jaffrennou P, Claudon J, Bazin M, Malik N S, Reitzenstein S, Worschech L, Kamp M, Forchel A and Gerard J M 2010 *Appl. Phys. Lett.* **96** 071103

[12] Yang Y D, Huang Y Z, Guo W H, Lu Q Y and Donegan J F 2010 *Opt. Express* **18** 13057

[13] Munsch M, Claudon J, Malik N S, Gilbert K, Grosse P, Gerard J M, Albert F, Langer F, Schlereth T, Pieczarka M M, Hofling S, Kamp M, Forchel A and Reitzenstein S 2012 *Appl. Phys. Lett.* **100** 031111

[14] Yang Y D, Xiao J L, Liu B W and Huang Y Z 2015 *J. Opt. Soc. Am. B* **32** 439

[15] Long H, Yang W, Ying L Y and Zhang B P 2017 *Chin. Phys. B* **26** 054211

[16] Nockel J U and Stone A D 1997 *Nature* **385** 45

[17] Chern G D, Tureci H E, Stone A D, Chang R K, Kneissl M and Johnson N M 2003 *Appl. Phys. Lett.* **83** 1710

[18] Wiersig J and Hentschel M 2008 *Phys. Rev. Lett.* **100** 033901

[19] Song Q H, Ge L, Stone A D, Cao H, Wiersig J, Shim J B, Unterhinninghofen J, Fang W and Solomon G S 2010 *Phys. Rev. Lett.* **105** 103902

[20] Levi A F J, Slusher R E, Mccall S L, Glass J L, Pearton S J and Logan R A 1993 *Appl. Phys. Lett.* **62** 561

[21] Boriskina S V, Benson T M, Sewell P and Nosich A I 2006 *IEEE J. Sel. Top. Quantum Electron.* **12** 52

[22] Jin X, Yang Y D, Xiao J L and Huang Y Z 2015 *IEEE J. Quantum Electron.* **51** 6500208

[23] Wang X Y, Chen H Z, Li Y, Li B and Ma R M 2016 *Chin. Phys. B* **25** 124211

[24] Yang Y D, Wang S J and Huang Y Z 2009 *Opt. Express* **17** 23010

[25] Song Q H, Ge L, Redding B and Cao H 2012 *Phys. Rev. Lett.* **108** 243902

[26] Yang Y D, Zhang Y, Huang Y Z and Poon A W 2014 *Opt. Express* **22** 824

[27] Wang S J, Lin J D, Huang Y Z, Yang Y D, Che K J, Xiao J L, Du Y and Fan Z C 2010 *IEEE Photon. Technol. Lett.* **22** 1349

[28] Poon A W, Courvoisier F and Chang R K 2001 *Opt. Lett.* **26** 632

[29] Huang Y Z, Guo W H and Wang Q M 2001 *IEEE J. Quantum Electron.* **37** 100

[30] Guo W H, Huang Y Z, Lu Q Y and Yu L J 2003 *IEEE J. Quantum Electron.* **39** 1563

[31] Wiersig J 2003 *Phys. Rev. A* **67** 023807

[32] Yang Y D and Huang Y Z 2007 *Phys. Rev. A* **76** 023822

[33] Wang S J, Huang Y Z, Yang Y D, Hu Y H, Xiao J L and Du Y 2010 *Chin. Phys. Lett.* **27** 014213

[34] Huang Y X, Qiu W B, Lin S X, Zhao J, Chen H B, Wang J X, Kan Q and Pan J Q 2016 *Sci. Chin. Inform. Sci.* **59** 042413

[35] Guo W H, Huang Y Z, Lu Q Y and Yu L 2004 *IEEE Photon. Technol. Lett.* **16** 479

[36] Huang Y Z, Chen Q, Guo W H, Lu Q Y and Yu L J 2006 *IEEE J. Sel. Top. Quantum Electron.* **12** 59

[37] Yang Y D and Huang Y Z 2007 *IEEE J. Quantum Electron.* **43** 497

[38] Yang Y D, Huang Y Z and Wang S J 2009 *IEEE J. Quantum Electron.* **45** 1529

[39] Huang Y Z, Guo W H and Wang Q M 2000 *Appl. Phys. Lett.* **77** 3511

[40] Moon H J, An K and Lee J H 2003 *Appl. Phys. Lett.* **82** 2963

[41] Fong C Y and Poon A W 2004 *Opt. Express* **12** 4864

[42] Huang Y Z, Chen Q, Guo W H and Yu L J 2005 *IEEE Photon. Technol. Lett.* **17** 2589

[43] Chen Q, Yang Y D and Huang Y Z 2007 *Opt. Lett.* **32** 967

[44] Hattori H T, Liu D Y, Tan H H and Jagadish C 2009 *IEEE Photon. Technol. Lett.* **21** 359

[45] Liu D Y, Hattori H T, Fu L, Tan H H and Jagadish C 2010 *J. Phys. D: Appl. Phys.* **43** 135102

[46] Ma R M, Oulton R F, Sorger V J, Bartal G and Zhang X A 2011 *Nat. Mater.* **10** 110

[47] Bittner S, Bogomolny E, Dietz B, Miski-Oglu M and Richter A 2013 *Phys. Rev. E* **88** 062906

[48] Lee C W, Wang Q, Lai Y C, Ng D K T and Ng S K 2014 *IEEE Photon. Technol. Lett.* **26** 2442

[49] Bittner S, Lafargue C, Gozhyk I, Djellali N, Milliet L, Hickox-Young D T, Ulysse C, Bouche D, Dubertr R, Bogomolny E, Zyss J and Lebental M 2016 *Europhys. Lett.* **113** 54002

[50] Huang Y Z, Che K J, Yang Y D, Wang S J, Du Y and Fan Z C 2008 *Opt. Lett.* **33** 2170

[51] Yang Y D and Huang Y Z 2016 *J. Phys. D: Appl. Phys.* **49** 253001

[52] Guo W H, Huang Y Z, Lu Q Y and Vu L J 2003 *IEEE J. Quantum Electron.* **39** 1106

[53] Guo W H, Huang Y Z, Lu Q Y and Yu L J 2004 *Chin. Phys. Lett.* **21** 79

[54] Yang Y D, Huang Y Z and Chen Q 2007 *IEEE Photon. Technol. Lett.* **19** 1831

[55] Long H, Huang Y Z, Ma X W, Yang Y D, Xiao J L, Zou L X and Liu B W 2015 *Opt. Lett.* **40** 3548

[56] Weng H Z, Huang Y Z, Yang Y D, Ma X W, Xiao J L and Du Y 2017 *Phys. Rev. A* **95** 013833

[57] Tang M, Huang Y Z, Yang Y D, Weng H Z and Xiao Z X 2017 *Photon. Res.* **5** 695

[58] Liu B W, Huang Y Z, Long H, Yang Y D, Xiao J L, Zou L X and Du Y 2015 *IEEE Photon. Technol. Lett.* **27** 1853

[59] Liao M L, Huang Y Z, Weng H Z, Han J Y, Xiao Z X, Xiao J L and Yang Y D 2017 *Opt. Lett.* **42** 4251

[60] Weng H Z, Wada O, Han J Y, Xiao J L, Yang Y D, Huang Y Z, Li J, Xiong B, Sun C Z and Luo Y 2017 *Electron. Lett.* **53** 939

[61] Weng H Z, Huang Y Z, Ma X W, Wang F L, Liao M L, Yang Y D and Xiao J L 2017 *IEEE Photon. Technol. Lett.* **29** 1931

[62] Guo C C, Xiao J L, Yang Y D, Zhu Z H and Huang Y Z 2016 *IEEE Photon. Technol. Lett.* **28** 217

[63] Ding K, Liu Z C, Yin L J, Hill M T, Marell M J H, van Veldhoven P J, Noetzel R and Ning C Z 2012 *Phys. Rev. B* **85** 041301

[64] Ding K, Hill M T, Liu Z C, Yin L J, van Veldhoven P J and Ning C Z 2013 *Opt. Express* **21** 4728

[65] Hill M T, Marell M, Leong E S P, Smalbrugge B, Zhu Y C, Sun M H, van Veldhoven P J, Geluk E J, Karouta F, Oei Y S, Notzel R, Ning C Z and Smit M K 2009 *Opt. Express* **17** 11107

[66] Oulton R F, Sorger V J, Zentgraf T, Ma R M, Gladden C, Dai L, Bartal G and Zhang X 2009 *Nature* **461** 629

[67] Xiao Z X, Huang Y Z, Yang Y D, Tang M and Xiao J L 2017 *Opt. Lett.* **42** 3173

[68] Ma X W, Huang Y Z, Yang Y D, Xiao J L, Weng H Z and Xiao Z X 2016 *Appl. Phys. Lett.* **109** 071102

[69] Ma X W, Huang Y Z, Yang Y D, Weng H Z, Wang F L, Tang M, Xiao J L and Du Y 2017 *Opt. Lett.* **42** 2291